

Dynamic analysis of a smooth penetrometer free-falling into uniform clay

M. NAZEM*, J. P. CARTER*, D. W. AIREY† and S. H. CHOW†

The finite-element analysis of free-falling objects penetrating soil deposits is one of the most sophisticated and challenging problems in geomechanics. A robust numerical method will be described here for dealing with such complex and difficult problems. The approach is based on the arbitrary Lagrangian–Eulerian (ALE) method of analysis, the main features and challenges of which are described briefly in the paper. The ALE method is then employed to perform a parametric study of a perfectly smooth penetrometer free-falling into a uniform layer of clay, which deforms under undrained conditions. The effect of the mechanical properties of the clay soil on the penetration characteristics is presented, and an approximate, closed-form expression is derived for the dynamic penetration factor, N_{dp} . Comparisons are made between the deduced values of N_{dp} and published values of the conventional cone factor, N_c , and comparisons are made with experimental data to validate the approach.

KEYWORDS: numerical modelling; offshore engineering; shear strength; site investigation; soil/structure interaction

L'analyse aux éléments finis d'objets en chute libre pénétrant dans des dépôts de sol est un des problèmes les plus sophistiqués et difficiles de la géomécanique. La présente communication décrit une méthode numérique robuste pour résoudre des problèmes aussi complexes et difficiles. Cette approche est basée sur la méthode d'analyse Lagrangien-Eulérien arbitraire (ALE), dont les principaux problèmes et caractéristiques sont décrits brièvement. On utilise ensuite la méthode ALE pour effectuer une étude paramétrique d'un pénétromètre parfaitement lisse tombant dans une couche d'argile uniforme, qui se déforme dans des conditions non drainées. On présente l'effet des propriétés mécaniques du sol d'argile sur les caractéristiques de pénétration, et on dérive une expression à forme fermée pour le facteur de pénétration dynamique N_{dp} . On effectue des comparaisons entre les valeurs déduites de N_{dp} et des valeurs publiées du facteur de cone N_c , pour procéder ensuite à des comparaisons avec des données expérimentales pour valider cette approche.

INTRODUCTION

Penetrometers are widely used as in situ tools to evaluate the mechanical properties of soils. The static cone penetration test (CPT) is now a standard in situ procedure to explore both stratigraphy and the geotechnical properties of soil layers. This test is usually performed at a penetration rate that is fast enough that little, if any, of the excess pore water pressures developed in clay soils during penetration have sufficient time to dissipate, but on the other hand it is normally slow enough such that inertia forces may be ignored in the test interpretation. However, the static CPT cannot be used easily in situations where sites are relatively inaccessible, such as many seabed soil deposits, particularly in deep water. In these cases a free-falling penetrometer (FFP) can be employed to provide information on the strength of these sediments. Such tests can provide useful data, such as the total depth and time of penetration, and the deceleration characteristics of the falling penetrometer. Potentially, these data can then be used to deduce strength parameters for the soil in situ.

To date, dynamic penetrometers have been used for offshore oil and gas industry applications such as determining soil strengths for pipeline feasibility studies and anchoring systems, in military applications for naval mine counter-measures and terminal ballistic studies, and in extraterrestrial exploration, and they have also been proposed and investigated for deep-sea nuclear waste disposal (Chow, 2012). The specifications of a dynamic penetrometer, including its

shape, geometry, mass and initial velocity, normally depend on its application. For instance, torpedoes used to anchor flexible risers are typically 12–15 m long, weigh 240–950 kN in air, and are 762–1077 mm in diameter (Medeiros, 2002), and the STING penetrometer, developed by Canada's Defence Research Establishment Atlantic to investigate the upper seabed, consists of a steel rod 1 m long and 19 mm in diameter, with an enlarged tip at its base with diameters of 25–70 mm (Mulhearn, 2002). Numerical and experimental studies have shown that the penetration characteristics of these penetrometers depend on their geometry and impact energy, and also on the mechanical properties of the soil layer, particularly its undrained properties. Scott (1970), Dayal & Allen (1973), True (1975) and Beard (1977) are among the pioneers who presented the earliest applications of FFPs in providing information on the upper few metres of seabed sediments. At the time of these studies, powerful numerical methods were not available to solve the corresponding theoretical problem, and researchers had to rely on empirical correction factors to interpret test data. Scott (1970) also demonstrated that technological limitations prevented reliable data from being obtained. Over the last decade, improvements in sensor technology have led to renewed interest in the dynamic penetration resistance of soil, with several new penetrometer systems being developed to investigate soil strength and bearing capacity. One of the factors preventing the widespread use of this technology is the uncertainty in the method of interpretation. For example, field studies (Mulhearn, 2002; Abelev *et al.*, 2009) with penetrometers of different diameters have shown that the diameter affects the inferred soil strength, and have demonstrated the need for a better understanding of the factors affecting the dynamic soil resistance.

Numerous techniques have been proposed for estimating the undrained shear strength of clays based on the results obtained from various penetrometer systems. The earliest methods were necessarily empirical and analytical in nature,

Manuscript received 19 May 2010; revised manuscript accepted 21 March 2012. Published online ahead of print 23 July 2012.
Discussion on this paper closes on 1 March 2013, for further details see p. ii.

* Centre for Geotechnical and Materials Modelling, The University of Newcastle, Callaghan, Australia.

† Centre for Geotechnical Research, The University of Sydney, Australia.

and also relied on data obtained from experimental tests conducted in laboratories or at field sites (Beard, 1977; Freeman & Schuttenhelm, 1990; Bowman *et al.*, 1995). Because of the finite-element method's advantages, it has been widely used by many researchers over recent decades to analyse the static CPT, and recent developments in computing power have made it possible to model numerically objects penetrating into soil (e.g. Liyanapathirana, 2009; Sheng *et al.*, 2009; Carter *et al.*, 2010). The method has also been employed for the analysis of FFPs (Aubeny & Shi, 2006; Abelev *et al.*, 2009). The analysis of dynamic penetration is probably one of the most sophisticated and challenging problems in computational geomechanics. From the point of view of geometrical non-linearity, the penetration of objects into layers of soil usually involves severe mesh distortion caused by the large deformations. This usually motivates the application of sophisticated adaptive finite-element techniques, such as the arbitrary Lagrangian–Eulerian (ALE) method, which can successfully tackle problems that would otherwise involve severe mesh distortion and the entanglement of elements. Moreover, the analyst must also consider the relative incompressibility of the soil during the short testing periods required for full penetration, and the likelihood of inhomogeneity, non-linearity of the stress–strain behaviour, and the rate dependence of the soil's stiffness and strength. The presence of these features requires a robust stress-integration algorithm to evaluate the stresses accurately for a given strain field. Inertia effects may also be important in cases where the penetration occurs rapidly. The analyst must also be aware of the possible reflection of stress waves in a finite-element domain usually surrounded by fictitious, finite, rigid boundaries. More importantly, the boundary conditions of the problem do not remain constant during the analysis, since the contact surface between the penetrometer and the soil changes continuously during penetration. Finally, an advanced and robust time-integration scheme needs to be employed to predict the highly non-linear response of the soil accurately.

The finite-element method can handle both simple and complex constitutive soil models; it can also be used to solve problems with complicated geometries and boundary conditions, and yet can provide reasonably accurate results. However, mesh distortion and overlapping of elements are the main drawbacks of the common finite-element solution methods, such as the updated Lagrangian (UL) formulation, when used for large-deformation problems. Mesh distortion in zones with high stress and strain concentration, such as near a penetrating cone tip, is almost inevitable if the finite-element mesh is fine enough to achieve acceptable results. A naïve solution to avoid such mesh distortion could involve using a coarse mesh under the penetrometer, but this usually leads to significantly inaccurate results.

Two main strategies have been introduced into the finite-element method, to overcome mesh distortion in problems involving relatively large deformations; they are known as h-adaptivity and r-adaptivity. The h-adaptive finite-element method is based on the idea of generating a new, finer mesh, or subdividing the original elements in areas where the interpolation should be improved to achieve greater accuracy or to avoid mesh distortion. On the other hand, the r-adaptive finite-element method attempts to eliminate the mesh distortion by simply relocating the nodes in the finite-element domain. Unlike the h-adaptive technique, the r-adaptive strategy does not change the number of nodes or the connectivity of the elements. The most well-known and popular r-adaptive technique is probably the ALE method, which is based on the concept of separating the mesh displacements and the material displacements. This method will be explained in more detail in this paper.

As mentioned previously, if necessary, the h-adaptive finite-element method divides the problem domain into smaller elements, producing a new mesh, generally using the same type of elements as in the old mesh. Hu & Randolph (1998) proposed a successful numerical procedure to deal with mesh distortion by combining the conventional small-strain finite-element method with an automatic mesh-generation algorithm and a linear stress interpolation technique. They used this method to study plane-strain and axisymmetric problems such as cavity expansion and the bearing capacity of footings. They found this technique to be a practical approach, which can make good use of a small-strain finite-element code and yet provide accurate solutions for problems that involve large strains and large deformations. Randolph *et al.* (2008) presented some applications of the h-adaptive finite-element method in offshore engineering problems such as offshore foundations, surface penetration of pipelines and breakout capacity of plate anchors. Susila & Hryciw (2003) proposed a finite-element model based on a large-strain formulation and an auto-adaptive remeshing technique to study cone penetration in normally consolidated sand. They used the Mohr–Coulomb criterion to describe the frictional contact surface between the cone and the sand. The material behaviour was modelled by a non-associative Drucker–Prager model. Their model was implemented into ABAQUS, a commercial finite-element package, with an explicit time-stepping scheme that can simulate cone penetration.

The ALE method, being well established in fluid mechanics and solid mechanics, has been shown to be robust and efficient in solving a wide range of both static and dynamic geotechnical problems involving large deformations. Nazem *et al.* (2006) presented a robust mesh-optimisation procedure used with the operator-split technique for solving large-deformation problems in geomechanics. This technique refines a mesh by relocating the nodal points on all material boundaries, followed by a static analysis. Later, Nazem *et al.* (2008) presented an ALE formulation for solving elastoplastic consolidation problems involving large deformations. These authors compared the performance of the ALE method with the UL method, and showed the efficiency and robustness of the ALE method by solving some classical problems such as the consolidation of footings and cavity expansion. Sheng *et al.* (2009) addressed a successful application of the ALE method, incorporated with an automatic load-stepping scheme and a smooth contact discretisation technique, in solving geotechnical problems involving changing boundary conditions, such as penetration problems including the installation of piles. The application of the ALE method in the dynamic analysis of geotechnical problems was also addressed by Nazem *et al.* (2009a).

In this paper, an ALE method based on an implicit time-integration scheme is described for solving static and dynamic penetration of rigid objects into undrained soil layers. Key aspects of the method, including a new algorithm for nodal relocation, will be explained. Moreover, the performance and capability of the method are demonstrated by comparing the predictions obtained using this method with some experimental test results. This method is then employed to conduct a parametric study of an FFP. This study addresses the effects of the mechanical properties of the soil on the penetration characteristics of the FFP.

PROBLEM DEFINITION

In practice, an FFP can be released from a ship or a helicopter to impact on the soil on the seabed, in a swamp, or at any inaccessible sites. Onboard devices often monitor and record the penetration response, which is then used to

estimate the mechanical properties of the soil, to classify the soil, or to measure dredging quantities, etc. Fig. 1 depicts an FFP impacting on a soil layer, and in its final position at rest (zero velocity). The initial velocity of the FFP, its mass and its diameter are assumed to be v_0 , m and d respectively. Although a conical tipped penetrometer is shown in Fig. 1, the method presented here can be used for other types of object, such as spherical, annular or flat-tipped penetrometers, as experiments (Chow, 2012) have shown that the tip shape has minimal effects on the free-fall penetration. Note that p and t_p in Fig. 1 denote the total depth and the total time of penetration respectively. The soil is assumed to be undrained, incompressible and homogeneous, with the possibility of its mobilised shear strength varying with strain rate. Given the values of v_0 , m and d , and the mechanical properties of the soil, the finite-element method should be able to predict the penetration response and provide values of p and t_p for each case studied. As mentioned previously, the size of a penetrometer is usually a function of its application. In this study, attention is restricted to a range of relatively small penetrometers that weigh between 1 and 5 N and are 20–80 mm in diameter. Consequently, the behaviour of soils subjected to the penetration of larger objects, such as torpedo anchors, may require further investigation.

ARBITRARY LAGRANGIAN–EULERIAN METHOD

Operator-split technique

The ALE method has been developed to eliminate the mesh distortion that usually occurs in the UL method, by separating the material and mesh displacements. In a UL formulation, all variables are calculated at the end of the last equilibrium configuration. This assumption necessitates updating the spatial coordinates of all material points according to the incremental displacements at the end of each time step. Although the UL method is capable of solving some problems with relatively large deformations, it often fails to succeed, owing to the occurrence of excessive mesh distortion and the entanglement of elements. Mesh distortion usually starts with elements twisting or otherwise distorting out of their favourable shapes. For instance, in a domain consisting of triangular elements it is usually preferred that all triangles remain roughly equilateral during the analysis. However, material displacements, especially in regions with

higher deformation gradients, will gradually cause distortion of elements, decreasing the accuracy of the analysis or even ultimately resulting in a negative Jacobian. One way to overcome this shortcoming of the UL method is to separate the material and mesh displacements, leading to the development of the ALE method.

The equilibrium equation in the ALE method can be written in two different forms. It is possible to write the governing global system of equations in terms of two sets of unknown mesh and material displacements, leading to the so-called coupled ALE method. A supplementary set of equations in terms of the material and mesh displacements needs to be established through a mesh motion scheme, and the two sets of unknown displacements are then solved simultaneously. Alternatively, in the decoupled ALE method or the operator-split technique, the analysis can be performed in two separate steps: a UL step followed by a Eulerian step. In the UL step, the governing equations are only solved for the material displacements in order to fulfil the requirements for equilibrium. This step usually results in a distorted mesh. In the subsequent Eulerian step, the main goal is to minimise the mesh distortion by refining the mesh. Mesh refinement can be achieved by generating a new mesh for the entire domain, or by moving current nodal points into new positions. Regardless of which strategy is adopted for mesh refinement, the topology of the domain (i.e. the number of nodes, the number of elements, and the connectivity of elements) should not be changed. The Eulerian step is particularly important if significant mesh distortion occurs during the UL step.

After mesh refinement, all state variables at both nodal points and Gauss points must be mapped from the distorted mesh to the new mesh. This remapping is usually performed using a first-order expansion of Taylor's series as

$$\dot{f}^r = \dot{f} + (v_i - v_i^r) \frac{\partial f}{\partial x_i} \quad (1)$$

where \dot{f}^r and \dot{f} denote the time derivatives of an arbitrary function f with respect to the mesh and material coordinates respectively, v_i is the material velocity, and v_i^r represents the mesh velocity. The ALE method addressed in this paper is based on the operator-split technique presented by Nazem *et al.* (2006, 2008). Major aspects of the ALE method along with some of its new features, such as a procedure for nodal relocation, are discussed as follows.

Updated Lagrangian formulation

During each increment of the operator-split technique, the analysis starts with a UL procedure at time t . The main goal of the UL step is to find the incremental displacements, velocities and accelerations that will satisfy the equilibrium at time $t + \Delta t$. The matrix form of equilibrium is usually derived from the principle of virtual work. The weak form of this principle states that for any virtual displacement δu , equilibrium is achieved provided

$$\begin{aligned} \sum_k \left(- \int_{V_k} \sigma_{ij} \delta \varepsilon_{ij} dV_k - \int_{V_k} \delta u_i \rho \ddot{u}_i dV_k - \int_{V_k} \delta u_i c \dot{u}_i dV_k \right. \\ \left. + \int_{V_k} \delta u_i b_i dV_k + \int_{S_k} \delta u_i f_i dS_k \right) \\ + \int_{S_c} (t_N \delta g_N + t_T \delta g_T) dS_c = 0 \end{aligned} \quad (2)$$

where k is the total number of bodies in contact; σ denotes the Cauchy stress tensor; $\delta \varepsilon$ is the variation of strain due to

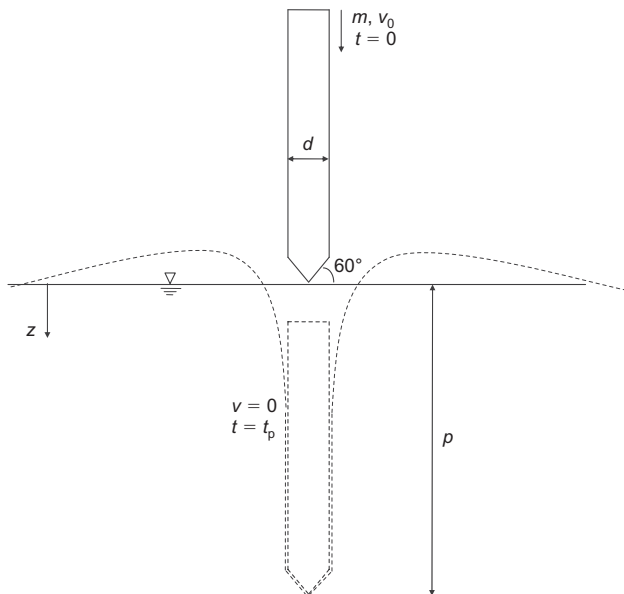


Fig. 1. Problem definition

virtual displacement, u , \dot{u} and \ddot{u} represent material displacements, velocities and accelerations, respectively; ρ and c are the material density and damping; b is the body force; q is the surface load acting on area S of volume V ; δg_N and δg_T are the virtual normal and tangential gap displacements; and t_N and t_T denote the normal and tangential tractions at the contact surface S_c . The solution of equation (2) requires the discretisation of the domain as well as the contact surfaces. In this study the so-called node-to-segment contact discretisation is adopted, as shown in Fig. 2, in which a node on the slave surface may come into contact with an arbitrary segment of the master contact surface. With this assumption the last two terms in equation (2), representing the virtual work due to normal and tangential contact forces, can be written in the form

$$\int_{S_c} t_N \delta g_N dS_c \approx \sum_{i=1}^{n_c} \delta u_i^T F_{N_i}^c \quad (3)$$

$$\int_{S_c} t_T \delta g_T dS_c \approx \sum_{i=1}^{n_c} \delta u_i^T F_{T_i}^c \quad (4)$$

in which n_c is the total number of slave nodes, and F_N^c and F_T^c represent the nodal forces of the contact element. The equation of motion for a solid can be obtained by linearisation of the principle of virtual displacement and is written in the following matrix form (e.g. Wriggers, 2006)

$$\mathbf{M}\ddot{\mathbf{u}}^{t+\Delta t} + \mathbf{C}\dot{\mathbf{u}}^{t+\Delta t} + \mathbf{R}^{t+\Delta t} = \mathbf{F}_{\text{ext}}^{t+\Delta t} \quad (5)$$

where \mathbf{M} and \mathbf{C} represent respectively the mass and damping matrices, \mathbf{R} is the stress divergence term, \mathbf{u} denotes the displacement vector, and \mathbf{F}_{ext} is the time-dependent external force vector. Note that the right superscript denotes the time when the quantities are measured, and a superimposed dot represents the time derivative of a variable. The solution of the momentum equation requires a step-by-step integration scheme in the time domain. Explicit and implicit methods are available for this purpose. In explicit methods the solution at time $t + \Delta t$ depends only upon known variables at time t . These methods, such as the central difference method, do not require factorisation of the effective stiffness matrix, and are easy to implement. However, explicit methods are conditionally stable, that is, the size of the time steps must be smaller than some critical time step. Implicit methods, on the other hand, require the solution of a non-linear equation at each time step, and have to be combined with another procedure, such as the Newton–Raphson method. The main advantage of implicit methods is that they can be formulated to be unconditionally stable, allowing the analyst to use a larger time step than in the explicit methods.

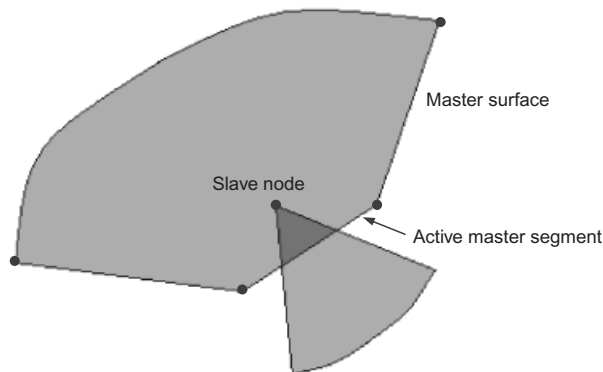


Fig. 2. Node-to-segment contact discretisation

In this study the implicit generalised- α method presented by Chung & Hulbert (1993) is adopted to integrate the momentum equation over the time domain. This method has been shown to be very efficient in solving dynamic problems in geomechanics (e.g. Kontoe *et al.*, 2008; Nazem *et al.*, 2009a). In the generalised- α method, two integration parameters, α_f and α_m , are introduced into the momentum equation to compute the inertia forces at time $t + (1 - \alpha_m)\Delta t$ and the internal and damping forces at time $t + (1 - \alpha_f)\Delta t$ respectively. The accelerations and velocities are approximated by Newmark equations according to

$$\begin{aligned} \ddot{\mathbf{u}}^{t+\Delta t} &= \frac{1}{\beta \Delta t^2} (\mathbf{u}^{t+\Delta t} - \mathbf{u}^t) - \frac{1}{\beta \Delta t} \dot{\mathbf{u}}^t - \frac{1 - 2\beta}{2\beta} \ddot{\mathbf{u}}^t \\ \dot{\mathbf{u}}^{t+\Delta t} &= \frac{\alpha}{\beta \Delta t} (\mathbf{u}^{t+\Delta t} - \mathbf{u}^t) + \left(1 - \frac{\alpha}{\beta}\right) \dot{\mathbf{u}}^t + \left(1 - \frac{\alpha}{2\beta}\right) \ddot{\mathbf{u}}^t \end{aligned} \quad (6)$$

where α and β are the Newmark integration parameters, and Δt represents the time step.

By introducing a tangential stiffness matrix

$$\mathbf{K}_T(\mathbf{u}_i^{t+\Delta t}) = \left(\frac{\partial \mathbf{R}}{\partial \mathbf{u}^{t+\Delta t}} \right)_{\mathbf{u}_i^{t+\Delta t}} \quad (7)$$

the Newton–Raphson method can be used to solve the momentum equation in the following form for the i th iteration

$$\begin{aligned} & \left[\frac{1 - \alpha_m}{\beta \cdot \Delta t^2} \cdot \mathbf{M} + \frac{\alpha(1 - \alpha_f)}{\beta \cdot \Delta t} \cdot \mathbf{C} + (1 - \alpha_f) \cdot \mathbf{K}_{T(i-1)} \right] \cdot \Delta \mathbf{u}_{(i)} \\ &= (1 - \alpha_f) \cdot \mathbf{F}_{\text{ext}}^{t+\Delta t} + \alpha_f \cdot \mathbf{F}_{\text{ext}}^t - (1 - \alpha_f) \cdot \mathbf{F}_{\text{int}(i-1)}^{t+\Delta t} \\ & \quad - \alpha_f \cdot \mathbf{K}_{T(i-1)} \cdot \mathbf{u}^t \\ & \quad - \mathbf{M} \left[\frac{1 - \alpha_m}{\beta \cdot \Delta t^2} \cdot (\mathbf{u}_{(i-1)}^{t+\Delta t} - \mathbf{u}^t) - \frac{1 - \alpha_m}{\beta \cdot \Delta t} \cdot \dot{\mathbf{u}}^t \right. \\ & \quad \left. - \left(\frac{1 - \alpha_m}{2\beta} - 1 \right) \cdot \ddot{\mathbf{u}}^t \right] \\ & \quad - \mathbf{C} \left\{ \frac{\alpha(1 - \alpha_f)}{\beta \cdot \Delta t} \cdot (\mathbf{u}_{(i-1)}^{t+\Delta t} - \mathbf{u}^t) \right. \\ & \quad \left. + \left[1 - \frac{\alpha}{\beta} (1 - \alpha_f) \right] \cdot \dot{\mathbf{u}}^t - \Delta t \left(\frac{\alpha}{2\beta} - 1 \right) (1 - \alpha_f) \cdot \ddot{\mathbf{u}}^t \right\} \\ & \mathbf{u}_{(i)}^{t+\Delta t} = \mathbf{u}_{(i-1)}^{t+\Delta t} + \Delta \mathbf{u}_{(i)}, \quad \mathbf{u}_{(0)}^{t+\Delta t} = \mathbf{u}^t \end{aligned} \quad (8)$$

where \mathbf{F}_{int} , the internal force vector, is obtained according to the Cauchy stress tensor, $\boldsymbol{\sigma}$, and the nodal forces at contact surfaces are obtained from

$$\mathbf{F}_{\text{int}}^{t+\Delta t} = \int_{V^{t+\Delta t}} \mathbf{B}^T \cdot \boldsymbol{\sigma}^{t+\Delta t} dV^{t+\Delta t} - \sum_{i=1}^{n_c} (\mathbf{F}_{N_i}^c + \mathbf{F}_{T_i}^c) \quad (9)$$

Note that the tangential stiffness matrix in equation (7) includes the contribution of the material stiffness, \mathbf{K}_{ep} , the stiffness due to geometrical non-linearity, \mathbf{K}_{nl} , and the stiffness due to normal and tangential contact, \mathbf{K}_{N_s} and \mathbf{K}_{T_s} ; that is

$$\mathbf{K}_T = \mathbf{K}_{\text{ep}} + \mathbf{K}_{\text{nl}} + \mathbf{K}_{N_s} + \mathbf{K}_{T_s} \quad (10)$$

In the problems studied here the penetrometer is idealised as a rigid body, that is, its size and shape remain unchanged during penetration. To achieve this condition all nodal points

on the FFP are prescribed as undergoing equal vertical displacements, while horizontal displacement is prohibited.

Definition of contact

To describe the contact at the interface between two bodies, constitutive equations must be provided for both the tangential and normal directions. Among several strategies available in contact mechanics, the penalty method is used to formulate these constitutive relations. The normal contact in the penalty method is described by

$$t_N = \varepsilon_N g_N \quad (11)$$

where ε_N is a penalty parameter for the normal contact.

In general, the response in the tangential direction is captured by the so-called stick and slip actions. In the former, no tangential relative movement occurs between the bodies, whereas the latter represents a relative displacement of bodies in the tangential direction. This assumption facilitates splitting the relative tangential velocity between the bodies, \dot{g}_T , into a stick part \dot{g}_T^{st} and a slip part \dot{g}_T^{sl} , as in the following rate form

$$\dot{g}_T = \dot{g}_T^{\text{st}} + \dot{g}_T^{\text{sl}} \quad (12)$$

The stick part can be used to obtain the tangential component of traction by

$$t_T = \varepsilon_T \dot{g}_T^{\text{st}} \quad (13)$$

where ε_T is a penalty parameter for tangential contact. Note that the assumption in (12) is analogous to the theory of plasticity, in which the incremental strains are divided into an elastic and a plastic part. Following this analogy, a slip criterion function must be provided. This can be achieved by writing the classical Coulomb friction criterion in the form

$$f_s(t_N, t_T) = \|t_T\| - \mu t_N \leq 0 \quad (14)$$

where μ is the friction coefficient.

For the numerical examples considered later in this paper, the interface between the penetrometer and the soil is assumed, for simplicity, to be perfectly smooth. This situation corresponds to the special case where $\mu = 0$.

Material behaviour

The undrained behaviour of the soil to be penetrated is represented by an elasto-plastic Tresca material model with an associated flow rule. In a large-deformation analysis, the stress–strain relations must be frame independent. This requirement, known as the principle of objectivity, can be satisfied by introducing an objective stress rate, such as the Jaumann stress rate $\dot{\sigma}^{\text{vj}}$, into the stress–strain relations as

$$d\sigma_{ij}^{\text{vj}} = \mathbf{C}^{\text{ep}}_{ijkl} \cdot d\epsilon_{kl} \quad (15)$$

where \mathbf{C}^{ep} represents the elasto-plastic constitutive matrix and ϵ is the strain vector. Among several available options to integrate equation (15), Nazem *et al.* (2009b) showed that it is slightly more efficient to apply rigid-body corrections during integration of the constitutive equations. This strategy is adopted in this study.

The undrained shear strength of cohesive soils often increases with the rate of straining. This phenomenon, termed the strain rate effect, usually introduces uncertainties in predicting the shear strength of soils in dynamic penetration tests. Graham *et al.* (1983) proposed a simple equation that prescribes approximately a 5–20% increase in shear strength for each order of magnitude increase in the rate of shear

strain. This effect can be expressed by the widely used equation

$$s_u = s_{u,\text{ref}} \left[1 + \lambda \log \left(\frac{\dot{\gamma}}{\dot{\gamma}_{\text{ref}}} \right) \right] \quad (16)$$

where s_u is the undrained shear strength of the clay, $s_{u,\text{ref}}$ represents a reference undrained shear strength measured at a reference strain rate of $\dot{\gamma}_{\text{ref}}$, $\dot{\gamma}$ denotes the shear strain rate, and λ is the rate of increase of strength per log cycle of time. Typically $\dot{\gamma}_{\text{ref}} = 0.01/\text{h}$ for clays (Einav & Randolph, 2006), and this value was adopted in the current study. For simplicity, the shear strength of a material can be assumed to be constant while integrating the constitutive equations during an individual time step of a non-linear finite-element analysis. However, the shear strength parameters must be updated according to the known shear strain rates at the end of each increment. Note that $\dot{\gamma}$ appearing in equation (16) should be evaluated using a frame-independent quantity such as the maximum plastic shear strain.

In CPTs it is found that the penetration resistance in clays increases as the rate of penetration (v) or the diameter of the penetrometer decreases. In static tests this is due mainly to partial consolidation occurring in advance of the cone tip, which in turn increases the effective stresses around the cone, followed by an increase of the sleeve friction. Usually a normalised velocity, V , is used to assess this degree of consolidation according to

$$V = \frac{vd}{c_v} \quad (17)$$

where c_v represents the coefficient of consolidation of the soil (e.g. Lehan *et al.*, 2009). Values of the normalised velocity between 10 (O'Loughlin *et al.*, 2004) and 100 (Brown & Hyde, 2008) have been recommended to ensure that the soil behaviour is undrained. In the problems studied here the value of normalised velocity is generally above 10 000, owing to the fast penetration of the object (see 'Parametric study' below) and the relatively short penetration time (0.1–0.9 s). Therefore undrained conditions are assumed throughout the penetration, and thus the shear strength increase due to partial consolidation is neglected.

Mesh refinement

In the ALE operator-split technique the material displacements are obtained at the end of the UL step, and will normally result in a distorted mesh. Refining the mesh at the beginning of each Euler step is very important, since a distorted mesh can lead to inaccurate results. Most mesh refinement techniques are based on special mesh-generation algorithms, which must consider various parameters such as the dimensions of the problem, the type of elements to be generated, and the regularity of the domain. Developing such algorithms for any arbitrary domain is usually difficult and costly. Moreover, these algorithms do not necessarily preserve the number of nodes or the number of elements in a mesh, and they may cause significant changes in the topology. A robust method for mesh refinement based on the use of a simple elastic analysis was presented by Nazem *et al.* (2006). The method has been implemented for both two-dimensional plane-strain problems and axisymmetric problems. To obtain the mesh displacements, it is necessary first to re-discretise all the boundaries of the problem, which include the boundaries of each discrete body, the material interfaces and the loading boundaries, resulting in prescribed values of the mesh displacements for the nodes on these boundaries. Each boundary node is then relocated along the boundary as necessary. With the known total displacements of these nodes

on the boundaries, an elastic analysis is then performed using the prescribed boundary displacements to obtain the mesh displacements for all the internal nodes, and hence the optimal new mesh. An important advantage of this mesh optimisation method is its independence of element topology and problem dimensions. The method does not require any mesh-generation algorithm, nor does it change the topology of the problem, and hence it can be easily implemented in existing finite-element codes. This method is potentially a good candidate for three-dimensional mesh optimisation.

The relocation of nodes along the boundaries plays a key role in the mesh refinement scheme proposed by Nazem *et al.* (2006). This relocation demands an efficient mathematical representation of the boundaries, which depends strongly on the physical problem being simulated. Nazem *et al.* (2008) proposed an efficient method for nodal relocation based on a quadratic spline technique. This method was successfully employed for solving many geotechnical problems, such as consolidation and bearing capacity of soils under a footing. However, it is not suitable for simulating boundaries in an FFP problem, owing to the linear shape of the penetrating object, which consequently introduces abrupt changes in the slope of the straight lines defining the boundary. Instead, a simpler, but more efficient, algorithm is introduced for nodal relocation along the boundary of the soil in contact with the penetrometer, which is based on the assumption of linear boundary segments. This procedure is depicted schematically in Fig. 3. The boundary between the soil and the penetrating object at the beginning of a time step (Fig. 3(a)) may become distorted after the UL step, as shown in Fig. 3(b). Such cumulative distortion, if not prevented, can potentially cause significant distortion of elements in that region, ultimately indicated by a negative Jacobian. Thus nodal relocation on the boundary can be performed, as shown in Fig. 3(c). Note that the nodes on a curved boundary are only permitted to move in the tangential direction of the boundary: that is, the normal component of the convective velocity on a boundary is zero, but not necessarily the tangential component. However, on a multi-linear boundary the nodes may be allowed to move along a line defining a linear segment. The nodal relocation on

linear segments is shown schematically in Fig. 4, where node i must be moved into a new position, i' , along line 1 or line 2 such that $l = l_i$. Note that l_i represents a normalised length of the segment, and can be calculated at the beginning of a time step before the mesh is distorted. The Cartesian coordinates of the new location can be calculated explicitly. For brevity, the full mathematical details are not provided here, but the procedure for relocating all nodes along a boundary is described in Algorithm 1, provided in the Appendix.

Energy-absorbing boundaries

One of the well-known issues in computational dynamic analysis of soil–structure interaction (SSI) problems is how to simulate an infinite medium. Employing the finite-element method, for instance, with boundaries that are not infinitely distant, one must guarantee that the outgoing waves from the source (usually a structure) do not reflect back from the finite boundaries toward the source, since in reality these waves should propagate to infinity and dissipate at a distance far from the source. If such reflection is allowed to occur, it will most probably affect the accuracy of the numerical results. To ensure that no waves are reflected back from truncated computational boundaries, it is common to use artificial boundaries that absorb the energy of incoming waves. A simple, but efficient boundary was developed by Lysmer & Kuhlemeyer (1969), which is known as the ‘standard viscous boundary’ in the literature. The standard viscous boundary is probably the most popular artificial boundary, since it possesses an acceptable dissipation characteristic at a low computational cost. Kellezi (1998) suggests that absorbing boundaries must not be located closer than $(1.2-1.5)\lambda_s$ (where λ_s is the length of the shear waves) from the excitation source. A recent study by Kontoe (2006) showed that the standard viscous boundary is capable of absorbing dilatational waves (P-waves) as well as shear waves (S-waves) in the analysis of plane-strain and axisymmetric SSI problems. When required, this type of boundary was used in the problems solved in this study.

PARAMETRIC STUDY

Introduction

The ALE method described in the previous section has been implemented in SNAC, a finite-element program developed for geotechnical research at the University of Newcastle, Australia. This code was used in all the finite-element analyses performed and reported in this study.

In order to analyse the FFP problem a finite-element mesh including 10 252 nodal points and 4988 elements was used,

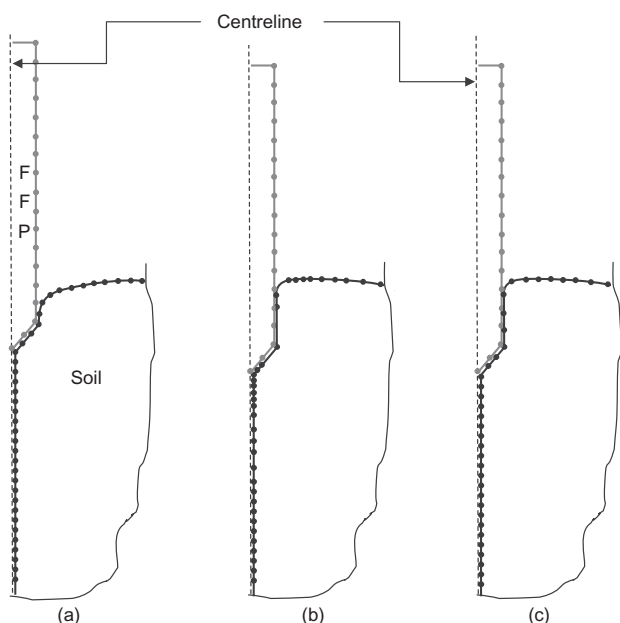


Fig. 3. Nodal relocation on boundary of FFP: (a) boundary element between soil and object before deformation; (b) distorted boundary; (c) boundary after nodal relocation

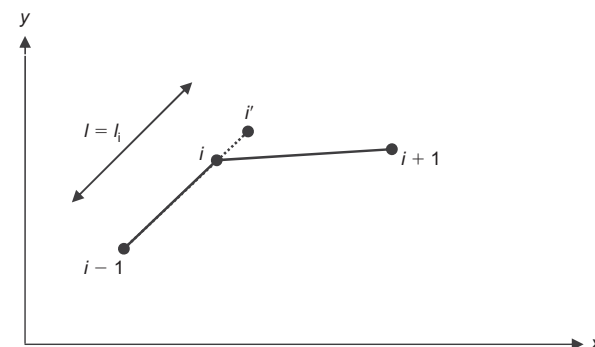


Fig. 4. Linear nodal relocation

as shown in Fig. 5. Note that, owing to axial symmetry, only one-half of the vertical cross-section of the problem is discretised by the finite-element mesh. All problems considered here were analysed using six-noded isoparametric triangular elements with six integration points. Owing to the incompressibility of most seabed soil deposits in the short term, Poisson's ratio, ν_u , was set equal to 0.49 (as an approximation of 0.5). E_u and G represent the undrained Young's modulus and shear modulus of the soil respectively. No material damping was assumed in the model. The right-hand and bottom boundaries of the problem domain (Fig. 5) are energy absorbent: that is, no wave reflection will occur, owing to the existence of the truncated finite-element boundaries, which are also considered rough and rigid. The size of each time step was generally 2×10^{-5} s. In cases where the impact velocity is relatively large, the size of the time step was assumed to be 1×10^{-5} s.

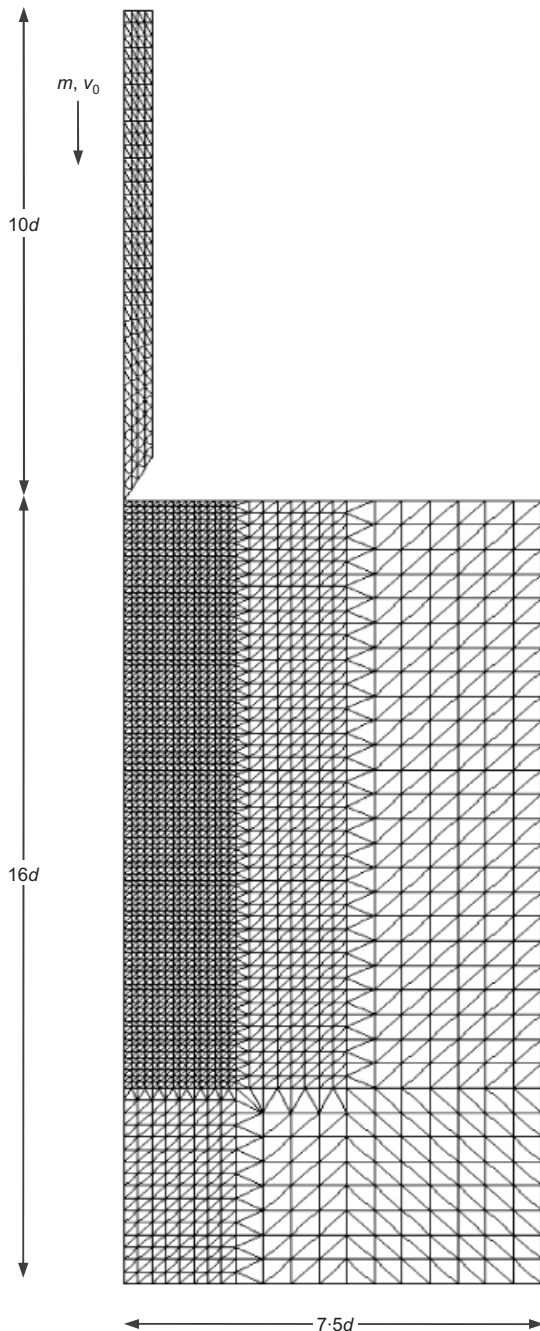


Fig. 5. Finite-element mesh of free-falling penetrometer

Validation of the ALE method

Previously, Carter *et al.* (2010) reported validation of the finite-element results predicted by SNAC through comparison of the predictions with experimental test results undertaken at the University of Sydney, Australia (Chow, 2012). These tests involved model penetrometers being dropped into pots of normally consolidated clay with constant undrained shear strength, some of which are represented in Table 1. This table also provides the results obtained from the ALE finite-element analysis, which were all conducted assuming $\lambda = 0.2$. Table 1 shows that there is generally good agreement between the experimental results and the numerical predictions.

Significance of mechanical properties

To study the effect of the mechanical properties of the soil on the penetration characteristics, a total of 223 cases were analysed using different values of m , v_0 , d , $s_{u,ref}$, $E_u/s_{u,ref}$ and λ . These values are listed in Table 2. In each case the finite-element method was used to predict the total depth and the total time of penetration, which varied between $1.16d$ and $17.92d$, and 0.005 s and 0.26 s, respectively. Note that in all analyses presented in this section it was assumed that the soil had uniform strength, and there was no friction developed between the soil and the penetrometer. The reason for ignoring the friction is that in the experimental tests the tip of the penetrometer was attached to a slender rod, the diameter of which was smaller than the diameter of the tip (usually a cone or a disc). Therefore the tip of the penetrometer came into contact with the soil only over a relatively small surface area, whereas the total contact area of the rod with the soil would have been negligible during penetration. The effect of shear strength increasing with depth as well as finite friction between the soil and the penetrometer on the penetration behaviour will be addressed in a future study.

It is notable that the assumption of undrained conditions can be validated by finding the minimum value of V for all cases considered in the parametric study. Assuming $c_v = 10^{-6} - 10^{-8}$ m²/s (typical values for coefficient of consolidation of clay), $d = 0.04$ m (minimum diameter), and $v = 2.5$ m/s (minimum average velocity), the value of the normalised velocity is calculated as 10^5 , which clearly shows that partial consolidation should not occur in the soils in which the penetrometers are embedded in this study.

To study the effect of the rate parameter λ and the stiffness-to-strength ratio, $E_u/s_{u,ref}$, on the depth of penetration the initial kinetic energy, normalised by $0.25\pi s_{u,ref} d^3$, has been plotted against the normalised penetration for all the tests. These plots are depicted in Figs 6, 7 and 8 for $E_u/s_{u,ref} = 100$, 200 and 500 ($G/s_{u,ref} \approx 33$, 67 and 167) respectively. It can be seen from these figures that an approximately linear relation exists between the normalised initial kinetic energy and the normalised total depth of penetration. This linear equation can be expressed in the form

$$\frac{\frac{1}{2} m v_0^2}{(\pi/4) s_{u,ref} d^3} = N_{dp} \left(\frac{p}{d} \right) \quad (18)$$

where N_{dp} , described here as the dynamic penetration factor, is given by

$$N_{dp} = A_{dp} - \frac{B_{dp}}{(p/d)} \quad (19)$$

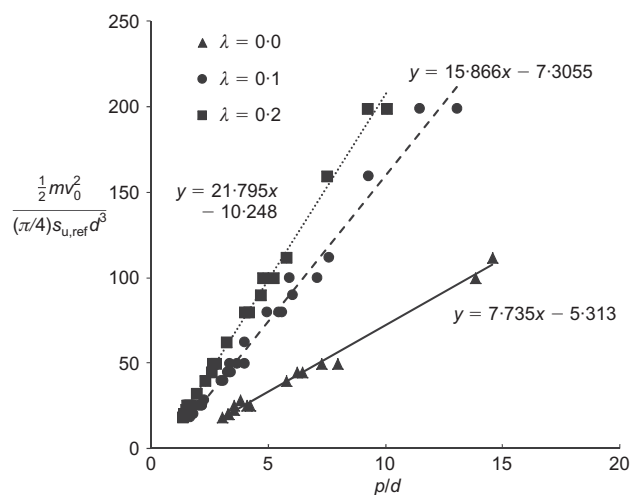
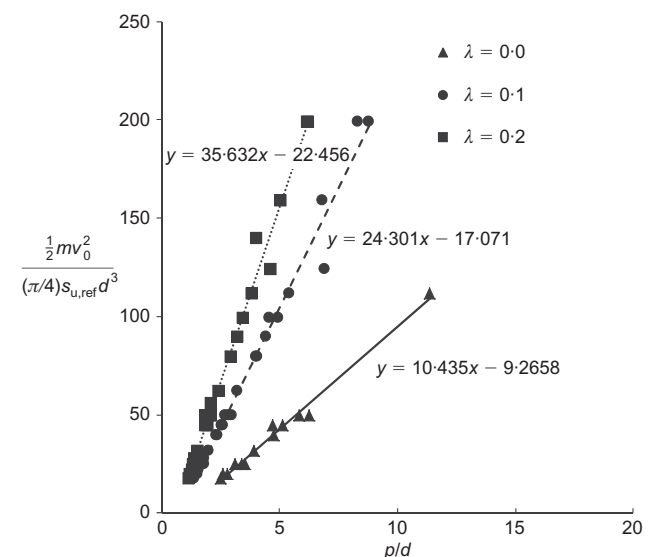
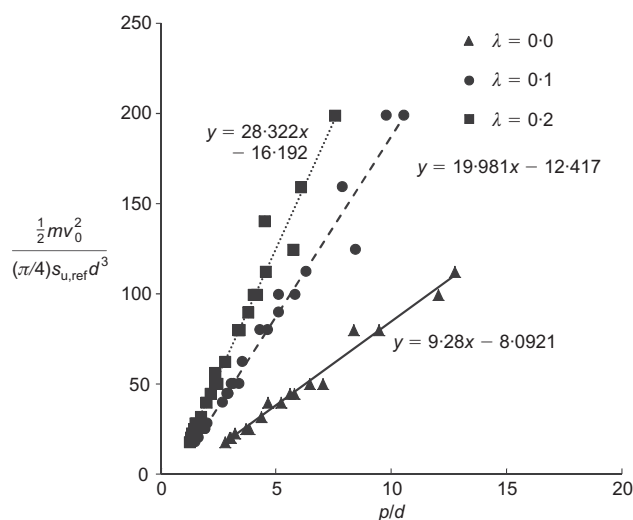
in which A_{dp} and B_{dp} are constants that depend on the rate parameter for strength, λ , and the rigidity index ($G/s_{u,ref}$), as

Table 1. Comparison between experimental results and ALE predictions

Test	$s_{u,ref}$: kPa	d : m	M : kg	v_0 : m/s	p/d (measured)	p/d (ALE)	Difference: ALE and tests: %
1	5.15	0.02	0.26	4.77	4.33	3.99	7.7
2	5.15	0.02	0.35	4.77	4.80	5.22	8.7
3	5.15	0.02	0.45	4.75	5.20	6.50	25.0
4	5.15	0.02	0.54	4.74	7.05	7.80	10.6
5	5.15	0.02	0.63	4.76	7.94	9.36	17.9
6	7.46	0.04	0.71	4.77	1.14	1.39	22.2
7	6.91	0.04	0.71	4.75	1.39	1.44	3.7
8	6.91	0.03	0.74	4.75	2.75	2.71	1.4
9	4.45	0.02	0.26	4.75	4.45	4.38	1.6

Table 2. Parameter values adopted in the analyses

Parameter	Values	Comment
d : m	0.04, 0.08	Typical values used in the tests
m : kg	0.1, 0.2, 0.5	Typical values used in the tests
v_0 : m/s	5, 10, 15, 20	Typical impact velocities
$s_{u,ref}$: kPa	1, 5, 10, 25	Representing a range of a very soft to soft soils
$E_u/s_{u,ref}$	100, 200, 500	Corresponding to $G/s_{u,ref} = 33, 67$ and 167 respectively, covering the typical range for soft soils
λ	0.0, 0.1, 0.2	To study the effect of the rate parameter

**Fig. 6. Normalised kinetic energy against normalised total depth of penetration for $E_u/s_{u,ref} = 100$ ($G/s_{u,ref} = 33$)****Fig. 8. Normalised kinetic energy against normalised total depth of penetration for $E_u/s_{u,ref} = 500$ ($G/s_{u,ref} = 167$)****Fig. 7. Normalised kinetic energy against normalised total depth of penetration for $E_u/s_{u,ref} = 200$ ($G/s_{u,ref} = 67$)**

shown in Tables 3 and 4 respectively. The values in these tables show that increasing the value of the rate parameter λ decreases the final penetration depth significantly, and this is because large values of λ correspond to soils that are effectively stronger during rapid undrained shearing.

Table 3. Values of dynamic penetration constant A_{dp} , deduced from finite-element studies

λ	$E_u/s_{u,ref}$ ($G/s_{u,ref}$)		
	100 (33)	200 (67)	500 (167)
0.0	7.74	9.28	10.44
0.1	15.87	19.98	24.3
0.2	21.80	28.32	35.63

Table 4. Values of dynamic penetration constant B_{dp} , deduced from finite-element studies

λ	$E_u/s_{u,ref} (G/s_{u,ref})$		
	100 (33)	200 (67)	500 (167)
0.0	5.31	8.09	9.27
0.1	7.31	12.42	17.07
0.2	10.25	16.19	22.46

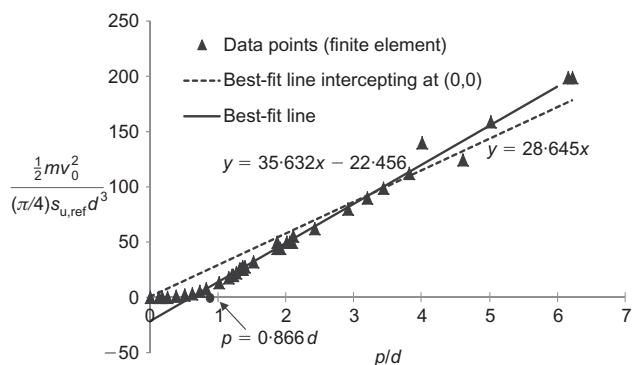
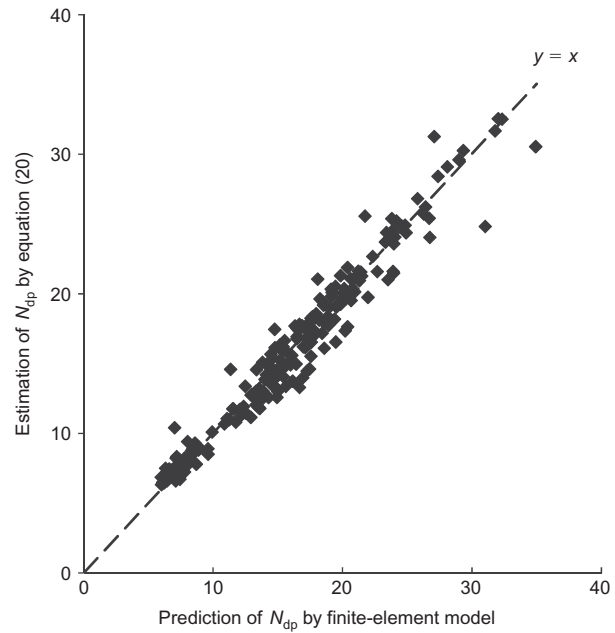
It is evident in Figs 6, 7 and 8 that the best-fit straight lines through the data points do not pass through the origin, even though from physical reasoning zero penetration is expected at zero impact energy provided the soil deformation under the static weight of the penetrometer is ignored. Indeed, the finite-element results reveal that the relationship between the normalised impact energy and the normalised penetration is not linear for values of penetration less than approximately $0.866d$, which corresponds to the point at which the tip of the cone just becomes fully embedded. The same non-linear relation may not exist for penetrometers with different tip shapes, such as a flat-tipped penetrometer, but this subject is yet to be investigated. This non-linear relation is illustrated in more detail in Fig. 9 for cases where $E_u/s_{u,ref} = 500$ and $\lambda = 0.2$. Similar plots have been obtained for other values of these parameters, but for brevity they are not presented here. As depicted in Fig. 9, the slope of the line passing the origin and the slope of the best-fit straight line are significantly different. In most practical problems the total depth of penetration will normally exceed $0.866d$, so that it is reasonable to accept the best-fit line as the more appropriate relationship between the normalised initial energy and the normalised penetration.

By a process of curve-fitting it has been possible to derive expressions for the variation of the dynamic penetration constants, A_{dp} and B_{dp} , with the rigidity index of the soil, $G/s_{u,ref}$, and the rate parameter that determines the soil strength, λ . These expressions are as follows

$$A_{dp} = 2.321 - 50.488\lambda + (1.690 + 34.546\lambda)\ln\left(\frac{G}{s_{u,ref}}\right) \quad (20)$$

$$B_{dp} = -2.698 - 148.36\lambda + 410.27\lambda^2 + (2.399 + 46.52\lambda - 103.91\lambda^2)\ln\left(\frac{G}{s_{u,ref}}\right) \quad (21)$$

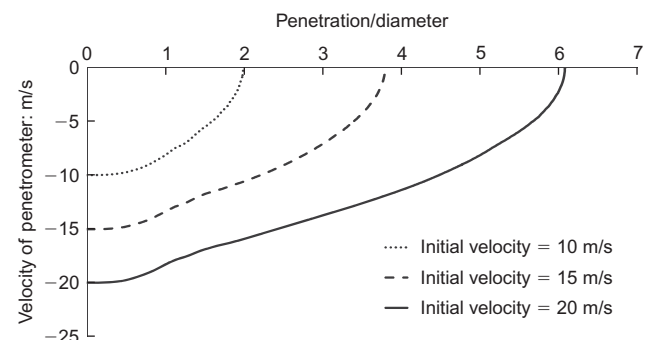
Figure 10 shows the values of N_{dp} deduced from the finite-element calculations for all 223 cases plotted against the

**Fig. 9.** Normalised kinetic energy against normalised total depth of penetration for $E_u/s_{u,ref} = 500$ ($G/s_{u,ref} = 167$) and $\lambda = 0.2$ **Fig. 10.** Comparison of values of the dynamic penetration factor N_{dp} , computed by finite-element model and by equation (20)

corresponding value of N_{dp} computed using equations (19)–(21). It can be seen that these equations provide reasonable estimates of the value of the dynamic penetration factor over the range of values of $G/s_{u,ref}$ and λ investigated, which clearly is convenient for use in geotechnical practice.

Deceleration characteristics

In order to study the deceleration characteristics of the penetrometer, its predicted vertical velocity is plotted against normalised penetration in Fig. 11 for selected cases. Among a wide range of results obtained in this study, plots are provided for the predictions where $d = 0.04$ m, $m = 0.2$ kg, $E_u/s_{u,ref} = 200$, $s_{u,ref} = 5$ kPa and $\lambda = 0.2$. It is observed that an approximately parabolic relation exists between the velocity of the penetrometer and its penetration of the soil. The existence of such parabolic relations can be verified by plotting the vertical velocity of the penetrometer against the time of penetration, as shown in Fig. 12 for the same set of predictions. Although the velocity is predicted to decrease non-linearly with time before the penetration reaches $0.866d$ (i.e. the time at which the tip of the cone just becomes embedded), Fig. 12 shows that the vertical velocity of the penetrometer decreases linearly with time as it penetrates further into the soil. This important observation suggests that the penetrometer decelerates at a constant rate, a_p , through-

**Fig. 11.** Velocity against penetration for $d = 0.04$ m, $m = 0.2$ kg, $E_u/s_{u,ref} = 200$, $s_{u,ref} = 5$ kPa, $\lambda = 0.2$

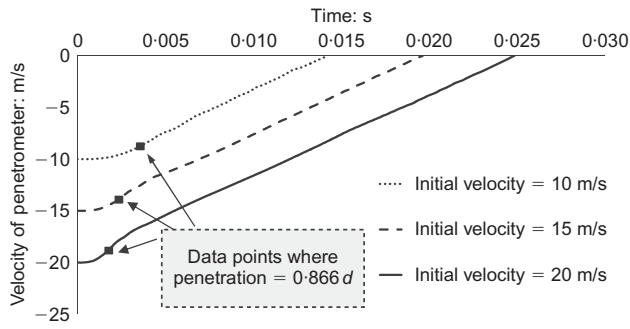


Fig. 12. Velocity against time for $d = 0.04$ m, $m = 0.2$ kg, $E_u/s_{u,ref} = 200$, $s_{u,ref} = 5$ kPa, $\lambda = 0.2$

out most of its penetration, which can then be estimated from rigid body dynamics as

$$a_p = -\frac{v_0}{t_p} = -\frac{v_0^2}{2p} \quad (22)$$

The approximately linear reduction of velocity with time was also observed in experimental studies with a free-falling flat-ended penetrometer, as depicted in Fig. 13 (Chow, 2012). Fig. 13(a) shows a comparison of the measured average deceleration with that predicted from equation (22) from the measured impact velocities and penetrations. Moreover, Fig. 13(b) provides the plots of velocity against time for experimental tests where $d = 0.02$ m, $m = 0.3$ kg, $s_{u,ref} = 10$ kPa and $\lambda = 0.3$. In all cases, an approximately linear reduction of the velocity with time can be observed. Evidently, the assumption of a constant deceleration throughout most of the penetration is also supported by the experimental data. Thus equation (22) provides a reasonably accurate estimate of the deceleration of an FFP in uniform clay.

It is interesting to note that constant decelerations have also been reported in numerical simulations of the penetra-

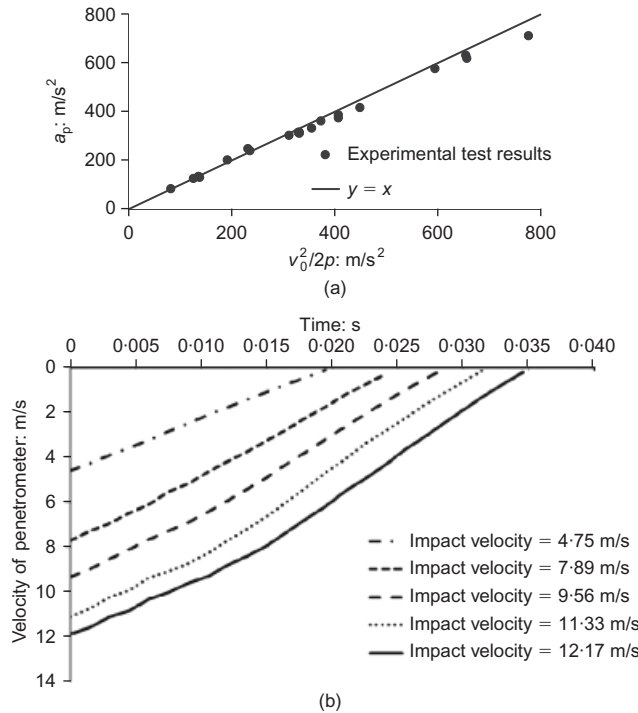


Fig. 13. Experimental verification of constant deceleration: (a) observed relationship between average acceleration, impact velocity and total penetration; (b) velocity against time plot from experiments with $d = 0.02$ m, $m = 0.3$ kg, $s_{u,ref} = 10$ kPa

tion of rods into metal and concrete targets, provided the penetration velocity is below a critical value and the diameter of the hole created does not exceed the diameter of the penetrating rod (Rosenberg & Dekel, 2009).

Cone factors

In order to interpret the undrained strength from static CPTs, use is often made of a static cone factor, N_c , relating the net stress on the cone, q_{net} , to the undrained strength of the soil

$$q_{net} = N_c s_u \quad (23)$$

For the situation where the deceleration is constant, the factor N_{dp} appearing in equation (18) can be interpreted as a dynamic cone factor. Substituting equation (22) into equation (18) and solving for N_{dp} provides

$$N_{dp} = \frac{m|a_p|}{(\pi/4)d^2 s_{u,ref}} \quad (24)$$

Note that the product ma_p in equation (24) is the average net force applied to the penetrometer during penetration. In other words, ma_p represents the soil resistance under dynamic penetration. Using equation (24) and dividing the soil resistance by the cross-sectional area of the penetrometer, $\pi d^2/4$, the dynamic penetration resistance of the soil, q_{dyn} , is obtained according to

$$q_{dyn} = N_{dp} s_{u,ref} \quad (25)$$

The values of N_{dp} presented in equation (19) and Tables 3 and 4 can now be investigated by plotting the contact pressure between the soil and the smooth (frictionless) penetrometer, normalised by $s_{u,ref}$, (i.e. $q_{dyn}/s_{u,ref}$), against the normalised penetration (p/d), as shown in Fig. 14. Note that this contact pressure represents the dynamic soil resistance under rapid penetration or rapid loading rates. The plots in Fig. 14 indicate that there is a peak value of the soil resistance soon after first impact, arising mainly from the inertia effects corresponding to the dynamic impact of the penetrometers with the soil, followed by a more or less constant value that approaches $N_{dp} s_{u,ref}$.

According to equations (19), (20) and (21), the values of the dynamic penetration factor, N_{dp} , for the case of a smooth penetrometer penetrating deeply into a uniform layer of soil ($p/d \rightarrow \infty$) with $\lambda = 0$ can be obtained from

$$N_{dp} = 2.321 + 1.69 \ln \left(\frac{G}{s_{u,ref}} \right) \quad (26)$$

Various authors have previously published theoretical solutions for the static cone factor, N_c . For example, Yu *et al.* (2000) used a novel steady-state finite-element solution assuming the modified Cam-Clay soil model to deduce an expression for N_c , and Liyanapathirana (2009) adopted the ALE finite-element approach with a von Mises soil model to deduce an expression for N_c . The expressions they derived using these various approaches are as follows.

Yu *et al.* (2000):

$$N_c = 0.33 + 2 \ln \left(\frac{G}{s_{u,ref}} \right) \quad (27)$$

Liyanapathirana (2009):

$$N_c = 1.0 + 1.825 \ln \left(\frac{G}{s_{u,ref}} \right) \quad (28)$$

Figure 15 presents a comparison of the cone factors pre-

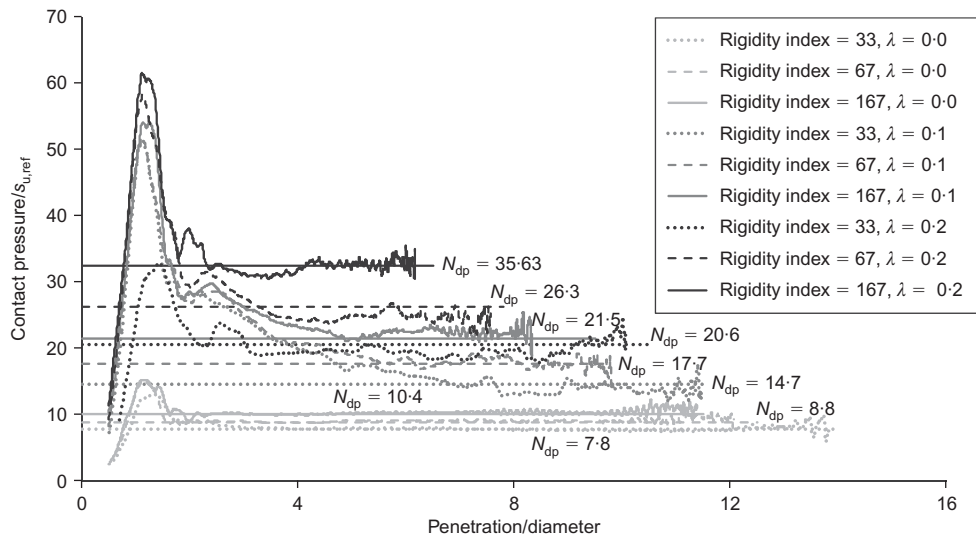


Fig. 14. Normalised contact pressure between penetrometer and soil plotted against penetration

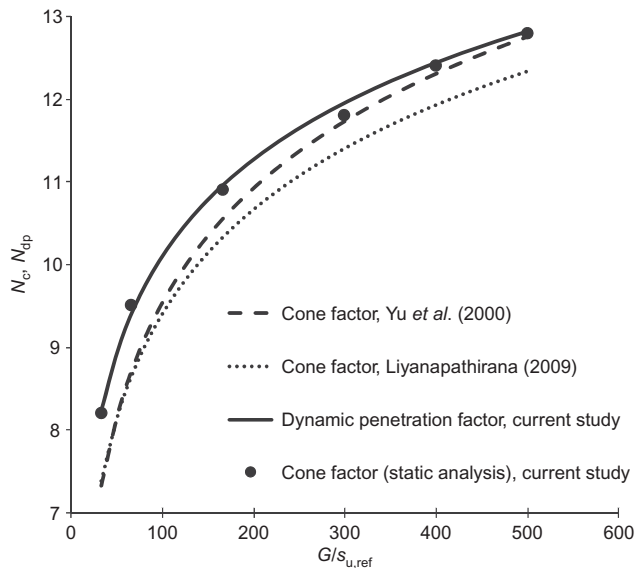


Fig. 15. Comparison of cone factor N_c and dynamic penetration factor N_{dp} for relatively deep penetrations and rate-insensitive soils ($\lambda = 0$)

dicted by equations (27) and (28), the dynamic penetration factor computed using equation (26), and values of the cone factor obtained by static analyses performed as part of this study. It can be seen that the values of the static cone factors obtained in this study are consistent with values of the dynamic penetration factor obtained from equation (26), but are slightly larger than the cone factors predicted by equations (26) and (28), apparently as a result of slight differences in the details and accuracy of the different finite-element models used for the analysis of static penetration.

From these results it can be inferred that after the initial shock of the first impact of the penetrometer with the soil, the inertia effects abate and penetration proceeds as if it were a static event, except that the resistance may be higher because of the effects of strain rate on undrained strength.

CONCLUSIONS

A robust ALE procedure was presented for analysing a penetrometer free-falling into a layer of uniform cohesive

soil. After validating the ALE method through comparison with experimental results, the method was used to investigate the effect of the soil properties on the penetration characteristics. Based on the problems solved, the following conclusions are obtained.

- By comparing the numerical and experimental test results, it was observed that the finite-element method can successfully tackle the problem of an FFP with sufficient accuracy and precision. This classical problem is generally regarded as one of the most sophisticated problems in computational geomechanics, owing to the non-linearities involved, which arise because of the large deformations, the highly non-linear behaviour of material, the changing boundary conditions, and the time-dependent and rate-dependent soil behaviour.
- The numerical results suggest that the total depth of penetration depends mainly on the initial kinetic energy of the penetrometer and its diameter, as well as on the mechanical properties of the soil, including mainly the rate parameter λ , and the rigidity index $G/s_{u,ref}$.
- The finite-element results show that for constant values of rigidity index and rate parameter a linear relation exists between the initial kinetic energy of penetrometer normalised by $0.25\pi s_{u,ref}d^3$ and the total penetration normalised by diameter. The parameter that relates these two quantities linearly was termed the dynamic penetration factor, N_{dp} , and it was found that its value depends on the rate parameter λ as well as the rigidity index of the soil. For the cases studied, the value of N_{dp} varied between about 8 and 35. The maximum value used for the normalised initial kinetic energy in this study was 200; the existence of such a linear relation for values of normalised energy greater than 200 is yet to be investigated.
- Based on the numerical analyses and experimental data, it was observed that the penetrometer decelerates at a constant rate during most of its penetration: that is, its velocity decreases linearly with time and quadratically with the depth of penetration. This important observation proves that the soil resistance under rapid penetration, or the dynamic bearing capacity of soil, can be estimated by multiplying its undrained shear strength, $s_{u,ref}$, by the dynamic penetration factor, N_{dp} .
- The results obtained here are valid for relatively small penetrometers, with a diameter between 0.04 m and

0.08 m, and may also depend on the mathematical model used to represent the strain rate effects (equation (16)), and its initial reference conditions. Accordingly, the dynamic penetration of larger objects, such as torpedo anchors, into clay soils requires further investigation.

ACKNOWLEDGEMENTS

Support for this research from the Australian Research Council is gratefully acknowledged.

APPENDIX

Algorithm 1: Linear nodal relocation across a boundary

1. Enter with the number of nodes on the boundary n , the global coordinates of each node (x_i and y_i), and the normalised lengths of the boundary segments l_i ($1 \leq i \leq n-1$).
2. Perform steps 3–9 for $i = 2$ to n .
3. Compute $l_1 = \sqrt{(x_i - x_{i-1})^2 + (y_i - y_{i-1})^2}$.
4. If $|l_1 - l_i| \leq \text{TOL} \times l_i$, then increase i and go to step 3.
5. If $l_1 > l_i$, set $x' = x_{i-1}$ and $y' = y_{i-1}$; otherwise set $x' = x_{i+1}$ and $y' = y_{i+1}$.
6. Compute $A = y' - y_i$, $B = x' - x_i$, and $C = x'y_i - y'x_i$.
7. If $|B| > \text{TOL}$, compute x_1 , y_1 , x_2 and y_2 from

$$D = B^2 [2B(Cy_{i-1} - Ax_{i-1}y_{i-1}) + B^2(l_i^2 - y_{i-1}^2) + A^2(l_i^2 - x_{i-1}^2) - C(C + 2Ax_{i-1})]$$

$$x_1 = \frac{-AC + B^2x_{i-1} - ABx_{i-1} + \sqrt{D}}{A^2 + B^2}, \quad y_1 = \frac{-C - Ax_1}{B}$$

$$x_2 = \frac{-AC + B^2x_{i-1} - ABx_{i-1} - \sqrt{D}}{A^2 + B^2}, \quad y_2 = \frac{-C - Ax_2}{B}$$

otherwise, find x_1 , y_1 , x_2 and y_2 according to

$$D = A^2 [-2A(Cx_{i-1} - Bx_{i-1}y_{i-1}) + A^2(l_i^2 - x_{i-1}^2) + B^2(l_i^2 - y_{i-1}^2) - C(C + 2By_{i-1})]$$

$$y_1 = \frac{A^2y_{i-1} - BC - ABx_{i-1} + \sqrt{D}}{A^2 + B^2}, \quad x_1 = \frac{-C - By_1}{A}$$

$$y_2 = \frac{A^2y_{i-1} - BC - ABx_{i-1} - \sqrt{D}}{A^2 + B^2}, \quad x_2 = \frac{-C - By_2}{A}$$

8. Find l' and l'' from

$$l' = \sqrt{(x_i - x_1)^2 + (y_i - y_1)^2}, \quad l'' = \sqrt{(x_i - x_2)^2 + (y_i - y_2)^2}$$

9. Compute new global coordinates of the i th node according to

$$x_i = x_2, \quad y_i = y_2 \quad \text{if } l' > l''$$

$$x_i = x_1, \quad y_i = y_1 \quad \text{if } l' \leq l''$$

10. Exit with the new global coordinates.

Note that the variable TOL in steps 4 and 7 is a parameter that determines whether nodal relocation is required, and its typical value is 10^{-10} .

NOTATION

A_{dp} , B_{dp}	dynamic penetration constants
a_p	deceleration rate of penetrometer
\mathbf{B}	strain matrix
b	body force
\mathbf{C}^{ep}	elasto-plastic constitutive matrix
c	material damping
c_v	coefficient of consolidation of soil
d	diameter of FFP
E_u	undrained Young's modulus of soil

\mathbf{F}_{ext}	external force vector
\mathbf{F}_{int}	internal force vector
$F_{N_i}^c, F_{T_i}^c$	nodal forces of contact element
f^r, f^s	time derivatives of arbitrary function f with respect to mesh and material coordinates respectively
G	shear modulus of soil
$G/s_{u,ref}$	rigidity index of soil
g_N	normal gap
\dot{g}_T	relative tangential velocity between bodies
$\dot{g}_T^{st}, \dot{g}_T^{sl}$	stick part and slip part of relative tangential velocity between bodies, respectively
\mathbf{K}_{ep}	material stiffness matrix
$\mathbf{K}_{Ns}, \mathbf{K}_{Ts}$	stiffness matrix due to normal and tangential contact
\mathbf{K}_{nl}	stiffness matrix due to geometrical non-linearity
\mathbf{K}_T	tangential stiffness matrix
k	total number of bodies in contact
\mathbf{M}, \mathbf{C}	mass and damping matrices
m	mass of FFP
N_c	static cone factor
N_{dp}	dynamic penetration factor
n_c	total number of slave nodes
p	total penetration depth
q	surface load
q_{dyn}	dynamic penetration resistance of soil
q_{net}	net stress on cone
\mathbf{R}	stress divergence term
s_u	undrained shear strength
$s_{u,ref}$	reference undrained shear strength
t	time
Δt	time step
t_N, t_T	normal and tangential tractions at contact surface S_c , respectively
t_p	total penetration time
u, \dot{u}, \ddot{u}	material displacements, velocities and accelerations, respectively
\mathbf{u}	displacement vector
V	normalised velocity
v	rate of penetration
v_i	material velocity
v_i^r	mesh velocity
v_0	initial velocity of FFP
x, y	Cartesian coordinates
α, β	Newmark integration parameters
α_f, α_m	integration parameters
$\dot{\gamma}$	shear strain rate
$\dot{\gamma}_{ref}$	reference strain rate
$\delta g_N, \delta g_T$	virtual normal and tangential gap displacements, respectively
$\delta \epsilon$	variation of strain
$\boldsymbol{\epsilon}$	strain vector
ϵ_N, ϵ_T	penalty parameters for normal and tangential contact, respectively
λ	rate of increase of strength per log cycle of time
λ_s	length of shear waves
μ	friction coefficient
ν_u	undrained Poisson's ratio
ρ	material density
$\boldsymbol{\sigma}$	Cauchy stress tensor
$\dot{\boldsymbol{\sigma}}^J$	Jaumann stress rate

REFERENCES

- Abelev, A., Simeonov, J. & Valent, P. (2009). Numerical investigation of dynamic free-fall penetrometers in soft cohesive marine sediments using a finite element approach. *Proceedings of the Oceans 2009 MTS/IEEE conference: Marine technology for our future: Global and local challenges*, Biloxi, pp. 1–8.
- Aubeny, C. P. & Shi, H. (2006). Interpretation of impact penetration measurements in soft clays. *J. Geotech. Geoenviron. Engng ASCE* **132**, No. 6, 770–777.
- Beard, R. M. (1977). *Expendable Doppler penetrometer*, Technical Report. Port Hueneme, CA, USA: Naval Construction Battalion Center.
- Bowman, L., March, R., Orenberg, P., True, D. & Herrmann, H. (1995). Evaluation of dropped versus static cone penetrometers

- at a calcareous cohesive site. *Proceedings of OCEANS '95 MTS/IEEE Conference: Challenges of our changing global environment*, San Diego, CA, pp. 1846–1858.
- Brown, M. J. & Hyde, A. F. L. (2008). High penetration rate CPT to determine damping parameters for rapid load pile testing. *Proc. 3rd Int. Conf. on Geotechnical and Geophysical Site Characterisation*, Taiwan, 657–663.
- Carter, J. P., Nazem, M., Airey, D. W. & Chow, S. W. (2010). Dynamic analysis of free-falling penetrometers in soil deposits. In *GeoFlorida 2010: Advances in analysis, modelling and design*, GSP 199, pp. 53–68. Reston, VA, USA: American Society of Civil Engineers.
- Chow, S. H. (2012). *Rate effects in free-falling penetrometer tests in clay*. PhD thesis, The University of Sydney, Australia.
- Chung, J. & Hulbert, G. M. (1993). A time integration algorithm for structural dynamics with improved numerical dissipation: the generalized- α method. *J. Appl. Mech.* **60**, No. 2, 371–375.
- Dayal, U. & Allen, J. H. (1973). Instrumental impact cone penetrometer. *Can. Geotech. J.* **10**, No. 3, 397–409.
- Einav, I. & Randolph, M. (2006). Effect of strain rate on mobilised strength and thickness of curved shear bands. *Géotechnique* **56**, No. 7, 501–504, <http://dx.doi.org/10.1680/geot.2006.56.7.501>.
- Freeman, T. J. & Schuttenhelm, R. T. E. (1990). A geotechnical investigation of a deep ocean site. In *Geotechnical engineering of ocean waste disposal* (eds K. R. Demars and R. C. Chaney), pp. 255–275. Philadelphia, PA, USA: ASTM.
- Graham, J., Crooks, J. H. A. & Bell, A. L. (1983). Time effects on the stress–strain behaviour of natural soft clays. *Géotechnique* **33**, No. 3, 327–340, <http://dx.doi.org/10.1680/geot.1983.33.3.327>.
- Hu, Y. & Randolph, M. F. (1998). A practical numerical approach for large deformation problems in soils. *Int. J. Numer. Anal. Methods Geomech.* **22**, No. 5, 327–350.
- Kellezi, L. (1998). *Dynamic soil–structure interaction: Transmitting boundary for transient analysis*. PhD thesis, Series R No. 50, Department of Structural Engineering and Materials, DTU, Lyngby, Denmark.
- Kontoe, S. (2006). *Development of time integration schemes and advanced boundary conditions for dynamic geotechnical analysis*. PhD thesis, Imperial College, University of London, UK.
- Kontoe, S., Zdravkovic, L. & Potts, D. M. (2008). An assessment of time integration schemes for dynamic geotechnical problems. *Comput. Geotech.* **35**, No. 2, 253–264.
- Lehane, B. M., O'Loughlin, C. D., Gaudin, C. & Randolph, M. F. (2009). Rate effects on penetrometer resistance in kaolin. *Géotechnique* **59**, No. 1, 41–52, <http://dx.doi.org/10.1680/geot.2007.00072>.
- Liyanapathirana, D. S. (2009). Arbitrary Lagrangian-Eulerian based finite element analysis of cone penetration in soft clay. *Comput. Geotech.* **36**, No. 5, 851–860.
- Lysmer, J. R. & Kuhlemeyer, L. (1969). Finite dynamic model for infinite media. *J. Engng Mech. Div. ASCE* **95**, No. EM4, 859–877.
- Medeiros, C. J. (2002). Low cost anchor system for flexible risers in deep waters, *Proc. 34th Ann. Offshore Technology Conf., Houston, TX*, paper OTC 14151.
- Mulhearn, P. J. (2002). *Influence of penetrometer probe tip geometry on bearing strength estimation for mine burial prediction*, TR 1285. Fishermans Bend, Australia: DSTO Aeronautical and Maritime Research Laboratory.
- Nazem, M., Sheng, D. & Carter, J. P. (2006). Stress integration and mesh refinement in numerical solutions to large deformations in geomechanics. *Int. J. Numer. Methods Engng* **65**, No. 7, 1002–1027.
- Nazem, M., Sheng, D., Carter, J. P. & Sloan, S. W. (2008). Arbitrary Lagrangian-Eulerian method for large-deformation consolidation problems in geomechanics. I. *J. Anal. Numer. Methods Geomech.* **32**, No. 9, 1023–1050.
- Nazem, M., Carter, J. P. & Airey, D. (2009a). Arbitrary Lagrangian-Eulerian method for dynamic analysis of geotechnical problems. *Comput. Geotech.* **36**, No. 4, 549–557.
- Nazem, M., Sheng, D., Carter, J. P. & Sloan, S. W. (2009b). Alternative stress-integration schemes for large deformation problems of solid mechanics. *Finite Elements Anal. Des.* **45**, No. 12, 934–943.
- O'Loughlin, C. D., Randolph, M. F. & Richardson, M. D. (2004). Experimental and theoretical studies of deep penetrating anchors. *Proc. Ann. Offshore Technology Conf., Houston, TX*, paper OTC 16841.
- Randolph, M. F., Wang, D., Zhou, H., Hossain, M. S. & Hu, Y. (2008). Large deformation finite element analysis for offshore applications. *Proc. 12th Int. Conf. of IACMAG, Goa*, 3307–3318.
- Rosenberg, Z. & Dekel, E. (2009). The penetration of rigid rods: revisited. *Int. J. Impact Engng* **36**, No. 4, 551–564.
- Scott, R. F. (1970). In-place ocean soil strength by accelerometer. *J. Soil Mech. Found. Div. ASCE* **96**, No. 1, 199–211.
- Sheng, D., Nazem, M. & Carter, J. P. (2009). Some computational aspects for solving deep penetration problems in geomechanics. *Comput. Mech.* **44**, No. 4, 549–561.
- Susila, E. & Hryciw, R. D. (2003). Large displacement FEM modelling of the cone penetration test (CPT) in normally consolidated sand. *Int. J. Numer. Anal. Methods Geomech.* **27**, No. 7, 585–602.
- True, D. G. (1975). *Penetration of projectiles into sea floor soils*, Technical Report R-822. Port Hueneme, CA, USA: Civil Engineering Laboratory, US Navy Construction Battalion Center.
- Wriggers, P. (2006). *Computational contact mechanics*, 2nd edn. Berlin, Germany: Springer-Verlag.
- Yu, H. S., Herrmann, L. R. & Boulanger, R. W. (2000). Analysis of steady state cone penetration in clay. *J. Geotech. Geoenviron. Engng ASCE* **126**, No. 7, 594–605.